Imaging of surface plasmon polariton fields excited at a nanometer-scale slit

Lingxiao Zhang, Atsushi Kubo, Leiming Wang, Hrvoje Petek, and Tamar Seideman

Phys. Rev. B **84**, 245442 — Published 22 December 2011

DOI: 10.1103/PhysRevB.84.245442

Imaging of Surface Plasmon Polariton Fields Excited at a Nanometer Scale Slit

Lingxiao Zhang,[1] Atsushi Kubo,[2,3] Leiming Wang,[3] Hrvoje Petek[3] and Tamar Seideman[1]

[1]*Departments of Chemistry and Physics, Northwestern University, Evanston, IL 60208*

[2]*Institute of Physics, University of Tsukuba, Tsukuba, Ibaraki 305-8571, Japan*

[3]*Department of Physics and Astronomy, and Petersen Institute of NanoScience and Engineering, University of Pittsburgh, Pittsburgh, PA 15260*

(Date: November 15, 2011)

Abstract

Nonlinear two-photon photoemission electron microscopy is used to image surface plasmon polariton (SPP) wave packets excited by an obliquely incident laser pulse (~10 fs) at a single slit fabricated in a thin silver film. We image the forward propagating polarization grating formed by the coherent superposition of the external excitation pulse and the SPP wave packet fields. By systematically varying the coupling slit width from sub- to multiple-wavelength scale, we observe a modulated increase of the grating intensity, which is phenomenologically accounted for by distinct contributions to the forward coupling efficiency from the incident to the SPP waves. Full-wave, vectorial finite-difference time-domain (FDTD) simulation of the experiments is in good agreement with the experimental observations and explains their origin. In particular, the FDTD simulation illustrates detailed spatial variation of the polarization grating as a function of the geometry of the slit under excitation by ultrafast laser pulses at an oblique incidence.

I. INTRODUCTION

Surface plasmon polaritons (SPPs) are electromagnetic modes of metal/dielectric interfaces with characteristics of charge density fluctuations within metals and optical fields within dielectrics.[1, 2] Smooth metal surfaces with nanofabricated asperities such as holes,[3, 4] ridges[5] and slits[6-18] can act as elements for coupling, reflecting, and refracting SPPs at metal/dielectric interfaces. The spatial disposition of the coupling structures can be arranged to perform specific coherent optical manipulation of SPP waves such as focusing, interfering, or waveguiding.[19-21] Because the SPP fields can propagate at speeds approaching that of light in vacuum and be guided at the nanometer scale in composite metal-dielectric nanostructures,[22] they have been considered as a potentially revolutionary technology for ultra-broadband signal transduction and processing in sub-wavelength scale optoelectronic circuits,[23] and for enhancing the efficiency of light harvesting in solar energy applications.[24]

At an atomically flat metal/vacuum interface, light incident from vacuum is reflected with nearly 100% efficiency through the collective screening response of the free electrons in a metal. Because of momentum mismatch between the external and the SPP fields, the coupling of light from vacuum into the SPP mode can occur only through a coupling structure that acts as an additional source of momentum. Frequently, the momentum is supplied by sub-wavelength scale asperities that exist naturally or can be fabricated by a variety of lithographic methods. Nanometer scale slits carved into smooth metallic films are one of the most fundamental structures that can be exploited as light-SPP couplers.[6-14] Even for such simple structures, however, what processes contribute to the scattering of the incident field into the SPP mode, as well as what defines the total field at a distant point from the coupling structure has been controversial.[25-29] Recent studies have demonstrated that the efficiency of light-SPP coupling sensitively depends on both the width and the thickness of the slit.[6-11] In these studies, continuous wave (cw) SPP fields are excited at the slit using either back illumination normal to the surface or a slit-groove geometry. Whereas the light-SPP coupling structures have been investigated with cw excitation, simulations using ultra-short light pulses in the ~10 fs pulse duration range, which span a broad spectral width, have been sparsely reported in the

literature.[30-32] Considering that SPP lifetimes and propagation lengths span the femtosecond temporal and nanometer spatial scales, applications of SPP fields in, for instance, plasmonic circuits,[33,34] would require precise measurement and simulation on the corresponding scales. Therefore, to assess the function of a single slit coupler in broadband SPP wave packet (WP) excitation, it is necessary to describe the fundamental physics of the incident and scattered fields at single slit structures subject to the excitation with ultrafast pulses at an oblique excitation geometry.[34-39]

In this paper, we investigate the SPP WPs excited at single slits formed in an 80 nm silver film by 10 fs light pulses with a 65^{o} angle of incidence. Experimental and theoretical studies are focused on the two-photon photoemission electron microscopy (2P-PEEM) imaging of the interference pattern between the incident light pulse and the excited SPP WPs. The effectiveness of 2P-PEEM imaging combined with femtosecond laser pulse excitation for studying nanoplasmonic effects has been established in various nanostructures.[40-42] In conjunction with experimental results, we utilize analytic wave propagation and finite-difference time domain (FDTD) simulations to show that both the finite-pulse duration and the oblique incidence angle play a significant role in determining the surface polarization interference patterns (polarization gratings). Therefore, simulations beyond cw illumination at a normal incidence are required to explain the experimental findings. We also show that in addition to Fabry-Pérot resonances, oblique incidence introduces new conditions for modulating the SPP excitation by varying the slit width. This paper is organized as follows: Section II describes the experimental measurements, Sec. III discusses the analytic model and the FDTD simulation, and Sec. IV presents and discusses the results. Conclusions are drawn in Sec. V.

II. EXPERIMENTAL MEASUREMENTS

The interaction of a near-UV light pulse with a nanostructured Ag film generates an SPP WP that propagates at the Ag/vacuum interface. The external light and excited SPP WP fields form a polarization grating within the illuminated area with a spatial period that reflects their amplitudes and wave vector (k-vector) difference.[41,43,44] We utilize 2P-

PEEM to record such interference patterns with sub-optical wavelength resolution that is made possible by photoelectron imaging. At the highest field-of-view the aberrations of the PEEM electron optics limit the resolution to <50 nm. PEEM creates a spatial image of the photoelectron yield resulting from the rectification of the total second-order nonlinear polarization excited in the Ag metal film.[35,45] The relative amplitude and phase between the external and SPP fields, which define the visibility of the polarization interference pattern, are established by the geometry of the excitation and the coupling structure, as well as the coherent electromagnetic response of the metal film.

In order to reveal the role of the geometry of the coupling structure, we study the SPP fields generated at single slit apertures with design widths ranging from 80 to 1420 nm. The structures are imprinted by focused-ion-beam etching of a silicon Si(100) wafer substrate. After the lithographic forming, the silicon sample is transferred into an ultrahigh vacuum (UHV) chamber, where further processing is performed by surface science methods: first, the native oxide layer is removed from the Si wafer by thermal annealing to 1200 K; next, a flat and smooth, polycrystalline 80-nm thick Ag film is deposited at 100 K sample temperature by electron beam evaporation;[46] and finally, the sample is transferred under UHV conditions to the attached PEEM chamber for the photoemission imaging measurements. Considering the 30 nm skin depth of Ag, the Ag film is grown to sufficient thickness to decouple the SPP field at the Ag/vacuum interface from the silicon substrate. All measurements are performed on the same sample containing multiple slit structures at room temperature. The slits of different widths are translated into the PEEM field-of-view by the attached sample stage.

Details of the experimental approach for ultrafast PEEM measurements have been described elsewhere.[35,47] A schematic of the excitation geometry is shown in Fig. 1(a). SPP pulses are excited by the second harmonic of a Ti:sapphire oscillator operating with a 90 MHz repetition rate; the frequency doubled pulses have ~10 fs duration and 400 nm center wavelength with typical energy of ~1 nJ/pulse. *p*-Polarized light incident at 65° from the surface normal is focused to an elliptical spot with a ~100 μm minor axis on the sample. Because the spot size is larger than the field-of-view of the PEEM, the excitation can be regarded as being homogeneous. The coupling slits are oriented with their length dimension [*z*-direction in Fig. 1(a)] orthogonal to the optical plane [*xy*-plane in Fig. 1(a)].

To illustrate PEEM imaging, Fig. 1(b) and 1(c), respectively, show images of a 200 nm wide slit sample excited by 4.9 eV photons from an Hg lamp incident from the right, and 3.1 eV (400 nm), femtosecond laser excitation incident from the left. In both cases the angle of incidence is $65 \pm 1°$ from the surface normal. The estimated error in the incidence angle, which impacts the polarization grating fringe spacing, reflects the precision of the optical alignment into the microscope and the production error of the apparatus. Figure 1(b) shows the surface morphology recorded by the PEEM through single-photon photoemission. The slit structure is visualized as a dark vertical line; the origin of the contrast is the shadow cast by the slit when irradiated by the obliquely incident light and projection of electron emission of variously inclined surfaces in the surface normal direction. The 2PP image in Fig. 1(c) shows a polarization grating excited at the slit coupler that propagates in the forward direction (to the right). Other than the oscillatory structure, there are no high-contrast features such as local hot spots. This shows that the Ag film is sufficiently smooth not to support localized plasmon resonances. After averaging the same image over the *z*-direction, the cross-sectional profile in Fig. 1(d) gives a quantitative measure of the propagation distance dependent 2PP signal intensity in the *x*-direction.

In order to explain PEEM imaging we examine how incident light pulses excite transient surface polarization waves at the Ag/vacuum interface and how these waves evolve in space and time. The components of the total polarization P_{total} excited in the sample can be separated into the local and nonlocal contributions. The local contribution $P_{light} = \varepsilon_0 \chi E(x,t)$ is attributed to the complex linear susceptibility (χ) of Ag and the instantaneous position and time dependent amplitude of the external electric field. The external light field is taken as a Gaussian pulse of 10 fs duration, which is comparable to the pulse shape characterized by autocorrelation of two-photon photoemission from a Ta surface.[35] The nonlocal polarization, P_{SPP}, represents the SPP-WP that is generated by the external field impinging on the slit structure; the WP propagates along the Ag/vacuum interface according to the corresponding complex dielectric wave vector in the $+x$ (forward) and $-x$ (backward) directions [See Fig. 1(a)]. Only the surface polarization is considered in the following analytical model and numerical simulations, because the 2PP process has high surface sensitivity that is defined by <5 nm electron escape depth.[48]

The photon energy, $\hbar\omega$, and the Ag sample work function, Φ, satisfy the relation $\hbar\omega < \Phi < 2\hbar\omega$; therefore, photoemission from the surface with 3.1 eV photons occurs primarily through a two-photon process that is proportional to the fourth-power of the total polarization field. The spatial and temporal modulation of the 2PP process, which was described previously,[36] suggests that the measured photoemission yield represents a coherent superposition of the P_{light} and P_{SPP} contributions of nearly equal amplitudes. Ergo, in the analytical model we assume the 2PP yield to be proportional to $P_{total}^4 = [P_{light}(x,t) + P_{spp}(x,t)]^4$.

The PEEM objective collects the 2PP signal from the entire field-of-view, which is typically 20 × 20 μm, and images the spatial distribution of photoemission current using a micro-channel plate (MCP)/phosphor/CCD camera system. Because electronic detection system is much slower than both the excitation pulse duration and the SPP WP dephasing, the PEEM images are proportional to a time integral of P_{total}^4, *i.e.*,

$$I_S(x) = \int_{-\infty}^{+\infty} P_{total}^4(x,t')dt' . \quad (1)$$

The ~11 ns interval between the excitation pulses ensures that each excitation pulse acts on the sample independently.

III. THEORY AND SIMULATIONS

A. Analytical model

In this section we introduce an analytical model to establish a qualitative understanding of the PEEM imaging of SPP WPs. When the P_{light} and P_{SPP} polarization waves overlap in space and time, their coherent superposition generates two polarization gratings on each side of the coupling slit. The polarization gratings are stationary from pulse-to-pulse, because the phase relationship between P_{light} and P_{SPP} is defined by the physical arrangement of the excitation and geometrical design of the coupling structure.

For simplicity, the model only treats the SPP-WP propagation and imaging; the slit coupling structures are assumed to be infinitely narrow and long line sources of SPP-WPs. From the coupling point, SPP-WPs are launched in both the forward and backward

directions; they travel subsequently at a $v_g = d\omega/dk$ velocity, which is determined by the dispersive and dissipative properties of the interface and the spectrum of the excitation field. As the SPP-WPs propagate, they deform and attenuate according to their frequency dependent complex propagation wave vector. Such propagation effects are taken into account rigorously in our analytical model, in as much as the SPP-WP spectrum replicates that of the excitation pulse. Geometrical effects of the slit structure, such as the thickness and width of the slit that define the coupling of SPP WP, are not accounted for. These are treated rigorously in the fully vectorial simulation introduced in the next subsection.

Adopting a simplified description of the surface fields by assuming continuous wave (*cw*) excitation, *i.e.*, ignoring the effects of dispersion, we can interpret the gratings as interference patterns between the external field and SPP wave with well-defined wavelength. The wavelength of the external λ_0=400 nm field projected onto the surface plane λ_x is $\lambda_x = \lambda_0 / \sin\theta = 441.35$ nm, whereas the wavelength or the SPP wave λ_{SPP} is given by the SPP wave vector k'_{SPP} through the relation $\lambda_{SPP} = 2\pi / k'_{SPP}$. The wave vector, $k'_{SPP} = \mathrm{Re}[\omega\sqrt{\varepsilon_m/(1+\varepsilon_m)}/c]$, is determined by the complex, frequency-dependent dielectric function of Ag, ε_m , and vacuum, which form the interface. At 400 nm, the values of ε_m= -4.10+0.33i, and therefore $\lambda_{SPP} = 348.25$ nm. We use the Drude model to describe the complex dielectric function for Ag $\varepsilon_m = \varepsilon(\infty) - \omega_D^2 / (\omega^2 + i\Gamma_D\omega)$, where $\varepsilon(\infty) = 7.0246$, $\omega_D = 1.5713\times10^{16}$ rad/s, and Γ_D=1.4003×10^{14} rad/s. This set of parameters is optimized to fit the optical constants of Johnson and Christy for bulk silver in the spectral range of 330 to 500 nm.[49,50]

Using these parameters we can estimate the spatial modulation intervals of the grating patterns for the forward and backward SPP propagation to be $\lambda^{+}_{beat} = 1.65 \pm 0.05$ μm, and $\lambda^{-}_{beat} = 195 \pm 1$ nm, where we have used $\lambda^{\pm}_{beat} = (\lambda^{-1}_{SPP} \mp \lambda^{-1}_{x})^{-1}$. The estimated error includes only the uncertainty of the incident angle of light. The forward polarization grating pattern is the primary experimental observable for comparison with the analytical model as well as the FDTD simulations. The backward grating pattern is at the limit of the

spatial resolution of the PEEM (~200 nm) under the conditions used to capture the forward propagation, and consequently, was not scrutinized in quantitative measurements.

Next we consider the effect of excitation of SPP-WP with the *finite duration* excitation pulse on the polarization grating patterns. In the following, we use a Fourier analysis model to simulate the SPP propagation, which is similar to the procedure in Ref. 36. For the pulsed excitation, the light-induced polarization is given by,

$$P_{light}(x,t) = \eta_1 \exp[-(t - x\sin(\theta)/c)^2/\tau^2]\exp[i\omega_0(t - x\sin(\theta)/c)], \quad (2)$$

where η_1 is a constant scaling factor, $\tau = 10/\sqrt{2\ln 2}$ fs is the duration of the Gaussian pulse intensity, and ω_0 is the carrier angular frequency. We assume that the external field induces a polarization at the flat surface of the sample that is proportional to its local amplitude; the free electrons in Ag screen and reflect the external field instantaneously. At the origin, x=0, defined as the edge of the right slit, the external field also couples to the SPP modes. Because the field is delivered in a short pulse, the SPP response is described by a WP,

$$P_{SPP}(0,t) = \eta_2 \exp[-t^2/\tau^2]\exp(i\omega_0 t + i\varphi), \quad (3)$$

where φ is the phase of $P_{SPP}(0,t)$ relative to P_{light} at the point of excitation, and η_2 represents the amplitude. The magnitude of φ can be experimentally determined from PEEM images. Because positions of beat maxima are determined by the initial phase difference between the P_{light} and P_{SPP}, φ could be estimated from the position of the first maximum of polarization gratings, x_{peak}, as

$$\varphi = (x_{peak}/\lambda_{beat})\cdot 2\pi. \quad (4)$$

The SPP WP propagates along the Ag/vacuum interface according to the dispersion relation $k_{SPP}(\omega) = k'_{spp}(\omega) + i\,k''_{SPP}(\omega)$, given by the dielectric function that has already been defined. Expressing Eq. (3) as a sum over the frequency components composing the excitation pulse $P_{SPP}(0,t) = \eta_2 \sum_i a_i \exp(i\omega_i t + i\phi_i)$, where a_i and ϕ_i are respectively the amplitude and the phase of the Fourier component corresponding to angular frequency ω_i at the point of excitation. Here, we assume that the coupling efficiency and phase change of different Fourier components in the original light pulse are the same as the excited SPP at x=0 (*i.e.*, the SPP WP retains the same Gaussian temporal profile as the incident light).

The coupling efficiency and the phase change can be extracted from the first interference peak position and height in the experimental data. The range of ω_i is defined by the spectral range of the 10 fs excitation pulse. To expand the original Gaussian excitation, we have used approximately 230 Fourier components. The propagation of the SPP WP is then modeled by

$$P_{SPP}(x,t) = \eta_2 \sum_i a_i' \exp(i\omega_i t + i\phi_i'), \tag{5}$$

where $a'_i = a_i \exp[-k''_{SPP}(\omega_i)x]$ and $\phi_i' = \phi_i + k'_{SPP}(\omega_i)x$.[34] We note that to the extent that the non-retarded, local dielectric function of a sample is known, the time evolution of SPP-WPs with any arbitrary distribution of amplitudes and phases can be calculated with Eq. (5). The PEEM image is then simulated by substituting Eqs. (2) and (5) into Eq. (1). To quantify the coupling efficiency of the external field into SPP-WP, we define β as the ratio of the respective amplitudes, *i.e.*, $\beta = \eta_2/\eta_1$. By comparing the observed grating patterns with the analytical model simulations, using β as a fitting parameter, we can estimate the β values for the measured beat pattern for each slit width *w*.

B. Numerical simulation

Although the general intensity profiles of the polarization gratings can be understood in terms of the interference between P_{light} and P_{SPP}, the analytic model provides no information on the role of the slit geometry. The information on the efficiency of coupling of the external field into SPP WP is empirically manifested in β, but to interpret the slit width dependence of β, we need further theoretical modeling. In addition to SPP excitation at an edge, surface asperities, such as grooves and slits can excite additional evanescent and radiative modes (Ref. 9) that can contribute additional terms to Eq. (5), and thereby influence the amplitude and phase of the SPP-WP. Therefore, fully vectorial calculations are essential to capture the role of the geometrical effects.

We perform a fully vectorial, time-dependent calculation using the FDTD method. Because the laser spot size far exceeds the total surface area of the slit, we consider a two-dimensional (2D) cross section in the plane formed by the incident electric field **E**

and its wave vector $\mathbf{k}^{inc}$, and regard the incoming laser beam as a *p*-polarized uniform plane-wave in the vicinity of 12 μm to each side of the slit. These considerations are shown in Fig. 2, which illustrates a schematic of the simulated system. The simulation is performed by a home-developed FDTD simulation code, where we have used a recently developed total field/scattered field (TF/SF) formalism to rigorously introduce an obliquely incident plane-wave into the 2D simulation.[51] In Fig. 2, the shaded area enclosed by the dashed rectangle is the TF region, whereas the remaining space is the SF region. The incident field is introduced at the TF/SF boundary (dashed rectangle) at each time step to match the fields in the TF and SF regions. The details of this formulation are published in Ref. 51. We point out that in our simulation the incident field distribution is obtained by the same setup as in Fig. 2 with the slit removed. This implies that the incident field already involves the reflection and refraction at the upper and lower interfaces of the Ag slab, thus allowing us to analyze the pure scattering effects caused by the slit.[52] In its presence, the outgoing scattered field emerges in the SF region and is effectively absorbed by a Uniaxial Perfectly Matched Layers (UPML; in between the outermost rectangles in Fig. 2) absorbing boundary condition.[53]

We have used two types of time profile for the magnetic field component of the incident plane-wave: the first is a cw source $H(t) = \sin(\omega_0 t)$, which is slowly ramped to a steady amplitude to avoid a leading wave front with high frequencies; and the second, is a Gaussian pulse $H(t) = \exp(-(t - t_{delay})^2 / \tau^2)\sin(\omega_0 t)$, where τ is the pulse width as defined in Eq. (2), and t_{delay}=3τ. For both fields $\omega_0 = 2\pi c / \lambda_0$, and the amplitude of the *H*-field is set to 1 A/m. Separate tests are performed to verify numerical convergence with the mesh size of $\Delta x = 2$ nm and time step of $\Delta t = 0.3\Delta x / c \approx 2$ as. Independent tests show the maximum reflection error from the UPML to be $\sim 10^{-4}$, which indicates that the outgoing waves are effectively absorbed. At the detection line (dashed-dotted horizontal line in Fig. 2) coincident with the top Ag/vacuum interface, we calculate the 2PP current relevant to PEEM experiment by Eq. (1). In FDTD simulations the total electric polarization is calculated by $P_{total} = \sqrt{P_x^2 + P_y^2}$.[54] The simulation run time is chosen such that P_{total} acquires a negligible value at the start and end of the simulation. As the polarization occurs within the material, the exact location of the detection line for calculating P_{total} is placed 1 nm

below the top surface, while its location is exactly at the top surface of the slab for calculating field components E_x, E_y, and H_z. The transmission through the slit is calculated by integrating the Poynting vector along the lower edge of the slit (dotted segment in Fig. 2),

$$\begin{aligned} T_{total} &= \int_{t_0}^{t} T(t')dt' \\ &= \int_{t_0}^{t}\int_{0}^{w} \boldsymbol{S}(x,t')\cdot\hat{n}\,dxdt' \\ &= -\int_{t_0}^{t}\int_{0}^{w} E_x(x,t')\,H_z(x,t')dxdt'. \end{aligned} \tag{6}$$

In the above, $T(t)$ is the instantaneous transmission at time t, $\boldsymbol{S}(x,t)$ stands for the Poynting vector, and $\hat{n}$ stands for the surface normal unit vector ($\hat{y}$ direction in Fig. 2). Within FDTD, we have calculated the fields E_x and H_z explicitly as a function of discrete time step n_t and spatial location (i, j), the integration in Eq. (5) is thus carried out by the following expression:

$$T_{total} = -\sum_{n_t=0}^{N_t}\sum_{i\in slit} E_x\Big|_i^{n_t} H_z\Big|_i^{n_t}, \tag{7}$$

where the sub- and super-scripts to the right of the vertical bar indicate the discrete space and time steps, respectively. In our simulation, it is ensured that at $n_t = 0$, the field values are zero. In addition, N_t is chosen to be large such that the integration converges (*i.e.*, the field values at the bottom of the slit ring down to a negligible value). A similar numerical procedure is described in Refs. 4, 12, and 55.

IV. RESULTS AND DISCUSSIONS

With the methodology developed in the previous section, we proceed to re-examine the experimental beat patterns already introduced in Fig. 1. Figures 1(c) and 1(d) show the damped polarization grating pattern extending in the $x>0$ direction from the right edge of the slit. The observed beat wavelength of ~1.6 μm is in good agreement with the prediction of λ_{beat}^{+} = 1.65 μm considering the PEEM measurement accuracy and the uncertainty in the dielectric function of Ag. The profile of the beat pattern is reasonably reproduced by the pulsed excitation model calculation shown in Fig. 1(e). For both

experiment and pulsed excitation simulation, the beat pattern nearly vanishes by x= 6 μm, which is considerably shorter than the calculated damping length for the cw excitation [dotted line in Fig. 1(e)]. This confinement of the grating near the coupling region results from both the damping of P_{SPP} and the limited overlap of P_{light} and P_{SPP} in space and time, as will be discussed in detail. The backward polarization grating with calculated λ_{beat}^{-} = 195 nm (for x<0) that is evident in the simulation, remains unresolved in the experimental data; it is responsible, however, for the raised baseline in the –x direction. This experimental feature is well reproduced when the simulated result is convolved with a suitable window function corresponding to the instrumental resolution (not shown).

Figure 3(a) shows a series of the experimental polarization gratings for the range of slit widths of 80–1420 nm. Overall, the beat intensity increases as the slit width widens, indicating an enhancement of the light-SPP coupling efficiency. To represent this general trend, peak intensities of the first beat maxima are plotted as a function of the slit width in Fig 3(b). As marked by arrows, the intensity of the polarization grating is modulated with a period of ~200 nm, corresponding to $\lambda_{peak} = n\lambda_0/2$, where n is a positive integer. This periodic enhancement of the coupling shows that in addition to the overall increase in the coupling efficiency with the slit width, there is an additional periodic modulation, which is suggestive of a Fabry-Pérot interference effect.

Figure 4(a) shows polarization grating pattern intensity profiles selected from the data in Fig. 3(a). These profiles show that in addition to the amplitude increase, the beat patterns change in shape as the slit width increases. The destructive interference minima relative to the maxima (the fringe visibility) become progressively shallower with increasing width. The maximum visibility is expected when $P_{SPP} \approx P_{light}$. Because only P_{SPP} *depends on* the slit width, the observed changes indicate that P_{SPP} is in general equal to or larger then P_{light} within a few wavelengths of the coupling structure. By contrast to the sensitivity of P_{SPP} amplitude on w, the phase of P_{SPP} (φ) defined in the Eq. (3) is rather insensitive. The value of φ is experimentally determined using the Eq. (4) as $(0.34 \pm 0.03) \times 2\pi$. With this value of φ, profiles of the polarization gratings are calculated by the analytical model taking only β as a free parameter. The results of calculations are shown in Fig. 4(b). Both changes in the intensity and the shape of the

beat patterns are well reproduced, which validates the analytical model. More importantly, both phase and amplitude of P_{SPP} are quantified: As the slit widens from 120 to 1420 nm, β increases from 0.9 to 2.9.

There have been both experimental[10,25] and theoretical[29,56,57] studies analyzing the relative phase between the external and SPP fields. Theoretical analyses predict a π phase shift between the normally incident light and the SPP waves launched from slit structures in metal films.[56,57] In our case, the phase difference between incident light and SPP clearly deviates from π, possibly because of the oblique light incidence, which changes the excitation condition at the slit. In addition, the oblique incidence condition modifies the slit width dependence of the light-SPP coupling efficiency. For the case of normally incident light, the coupling efficiency was found to be modulated with the periodicity close to λ_0, providing almost zero coupling efficiency when $w = n\lambda_0$ (n = 1, 2, …).[56,58] Furthermore, the contribution from Fabry-Pérot resonances was not visible. Our results are in strong contrast to these cases: The coupling efficiency increases as the slit width widens in the investigated range [dotted line in Fig. 3(b)], and is weakly modulated by the Fabry-Pérot resonances.

The analytical model of Section III.A cannot explain the width-dependent coupling efficiency, because the excitation of SPP is assumed to occur at a point source. To explicitly take into account the slit width effects, we proceed to discuss the results of FDTD simulation introduced in Section III.B, which are reported in Figs. 5-7.

In the main panel of Fig. 5(a), we plot the spatial distribution of the 2PP signal for a slit width of w=200 nm, *i.e.*, $\lambda_0/2$. The blue curve shows the time-averaged signal $\overline{P_{total}^4(x)}$ for cw excitation ($\lambda_0 = 400$ nm), whereas the red curve shows the time-integrated signal given by Eq. (1) for the pulsed excitation. Both curves are normalized to the value of the first peak to the right of the slit, and only data in the total field region ($-12.1<x<11.9$ μm) are shown. Several interesting features are predicted in Fig. 5(a). First, the calculated signal vanishes across the slit ($-200<x<0$ nm), as expected, because the polarization is zero in vacuum. At the left and right walls of the slit, the polarization is maximized due to the localization of the electric field at the sharp corners.[12,55]

Second, interference patterns are clearly seen in the variation of the signal as a function of x. The interference between the incident wave penetrating within the skin depth of the metal and P_{SPP} gives rise to interference patterns to the right and left of the slit, with respective lengths similar to λ_{beat}^{+} and λ_{beat}^{-} predicted by the analytical model. We note that both the model and the FDTD calculation predict interference to the left of the slit. The backward interference produced by the FDTD (pulsed) calculation is more localized than the forward interference, because of different overlap in space and time of the counter-propagating and co-propagating light and SPP-WPs, as will be elaborated; because the left SPP-WP is sampled over a shorter distance and time than the right WP, the beat wavelength is less influenced by dissipation and dispersion. Nevertheless, the peak-to-peak distances start to deviate from the results provided by the model and FDTD (cw) results, as indicated by arrow 4.

The third feature we observe in Fig. 5(a) is the mildly varying envelope modulating the interference pattern. This effect gives rise to the hump at arrow 2 (x=−5.3 μm) and the clamping at arrows 5 and 6 (x=9 μm). Additional simulations varying the Ag film thickness reveal the predominant cause for the slowly varying envelope is the interference between the upper and lower surfaces of the slab, particularly at the two walls of the slits where the SPP-WP is initially launched. In Fig. 5(a), the black curve shows the interference pattern under the same conditions of the blue curve, except the thickness of the slab is 200 nm. We observe that for slab thicknesses 200 nm the modulation of the envelope in the interference pattern vanishes. Additional simulations (not shown) reveal that the modulation of the envelope in the interference pattern vanishes as long as film thickness is larger than 120 nm although previously we have assumed that SPP propagations at the upper and lower surfaces are decoupled at 80 nm film thickness. Nevertheless, we observe in Fig. 5(a) that for 80 nm film thickness, the coupling effect introduces only a mild change of the interference pattern. We further note that although the fundamental cause of the slowly varying envelope is the finite thickness of the slab, other factors such as the slit width, incident angle, and pulse duration (in the case of pulsed excitation) also affect the shape of the slowly varying envelope, especially in the backward scattering direction. These effects are beyond the scope of this paper and will be addressed in a future publication.

Figure 1(e) and 5(a) show that there is considerable difference in the damping of the interference patterns between the cw and pulsed excitation cases. This is indeed the case when one compares the polarization grating observed by PEEM with femtosecond pulse excitation and interference patterns of similar origin that have been observed by near-field scanning optical microscopy employing cw excitation.[4,43,44,59] In measurements employing cw-laser excitation detecting linear light scattering processes, the decay length reflects mainly the propagation length of the P_{SPP} field. In the case of PEEM measurements using fs-laser as the excitation source, the decay length of the beat pattern is diminished both by the optical nonlinearity of the measurement, and by the finite overlap in space and time of the SPP and light WPs.

To further illustrate the dynamics responsible for the interference in the pulsed case, we plot in Fig. 5(b) the calculated photoemission signal $I_S(x,t)$ and the magnetic field $H_S(x,t)$ as functions of distance at the top surface of the silver slab at a time instance after the peak of the incident pulse passes the right edge of the slit. The plot verifies that both forward and backward scattered waves form individual WPs. We note in particular the different mechanisms for localization of the interference pattern to the left and right of the slit: To the left of the slit, the localization occurs because the backward scattering SPP wave travels in the opposite direction to the excitation pulse. By contrast, the interference pattern to the right of the slit is limited in extent because the forward scattering WP travels at a smaller group velocity $v_g = d\omega/dk$ than the incident WP, and hence their spatial overlap gradually decreases. Consequently, the interference pattern builds up on a shorter time scale to the left than to the right of the slit. Close inspection of the forward and backward scattering WPs in Fig. 5(b) reveals that the leading edge of the WP acquires a longer wavelength than the trailing edge. This is consistent with the SPP dispersion relation wherein v_g is larger for smaller k (or large λ).

Next we examine the role of the slit width in determining the SPP wave coupling efficiency. The red curve with superimposed dots in Fig. 6(a) shows the FDTD calculated interference signal strength I_S^{RP} of the first peak to the right of the slit as a function of the slit width, which clearly reproduces and explains the experimental width dependence shown in Fig. 3(b). In the experiment I_S^{RP} exhibits a general increasing trend

with increasing *w,* superimposed by a modulation with maxima at $w = n\,\lambda_0/2$ (*n* being a positive integer). The increasing trend of I_S^{RP} results from constructive interference at the right edge of the slit between the incident pulse and the cylindrical wave launched at the left wall of the slit (see Ref. 60 for a detailed discussion of the origin of cylindrical waves).

The green curve with superimposed squares in Fig. 6(a) shows that the horizontal FP modes have a dominant effect on the backward scattering signal I_S^{LP} (first interference peak to the left of the slit), which shows mainly an oscillation with a periodicity $\lambda_0/2$. The oscillation is slowly dampened and chirped for *w*>800 nm because the effective horizontal confinement between the two walls of the slit is reduced for a more extended cavity. The significant difference in the slit width dependence of I_S^{RP} and I_S^{LP} is due to the combined effects of the geometry of the slit (slab thickness $t = 80$ nm), the large oblique incident angle (65° from the normal), and the finite duration of the pulse.

The blue curve in Fig. 6(b) shows the total transmission normalized to the slit width T_{total}/w as a function of the slit width. A suppression of transmission through the slit at $w = n\,\lambda_0/2$ is clearly seen for *w*<800 nm. Loosely speaking, this indicates that the FP modes, when formed, can efficiently "store" energy in the cavity and couple it into the forward and backward scattered SPP waves (rather than transmit the energy through the slit). It is also seen that T_{total}/w continues to increase and reach a constant value for $w > 10\,\lambda_0$, where the cavity effect vanishes.

To further clarify the excitation of horizontal FP modes of the cavity, we plot, in Fig. 7, the field distribution in the vicinity of slits of various widths. Panels (a) and (c) correspond to the first and third FP modes, while panel (b) corresponds to an anti-resonant case. We only show the field components E_y and H_z because they entail a Poynting vector leading to horizontal cavity modes. In all panels, the tilted field distribution inside the slit and the asymmetric interference patterns at both the upper and the lower surfaces with respect to the slit center (*cf.* Fig. 5) arise from the oblique incidence of excitation field. Although the resonance condition is not immediately deducible from the field patterns, mainly because of the limited confinement by the 80 nm thick cavity and the oblique incidence, we still observe that H_z at the left edge of the

slit, highlighted by the dashed circles, oscillates and reaches its minima [maxima] for slit widths $w = n\lambda_0/2$ [$w = (n+\frac{1}{2})\lambda_0/2$] for $n \le 3$. H_z at the right edge of the slit, by contrast, does not show a strong modulation with varying slit width, as it depends predominantly on the strength of the incident field. These observations correlate with the results shown in Fig. 6, where the cavity modes only introduce minor modulation in the slit width dependence of I_S^{RP}, whereas they strongly modulate I_S^{LP}.

V. CONCLUSIONS

We utilized two-photon photoemission electron microscopy to image the surface plasmon wave packets excited by an ultrafast light pulse at a single slit in silver thin film. The PEEM images of the induced surface polarization reveal the coherent interference between the incident light pulse and the excited surface plasmon wave packets. By investigating a series of slits with different width, experiments with the same incidence condition show that the interference signal is enhanced by increasing the slit width from sub-wavelength scale (80 nm) to multiple wavelength scale (1420 nm) in addition to the enhancement due to the Fabry-Pérot resonances. This effect is accounted for by an increase of the forward coupling efficiency within an analytical model involving only the incident wave and forward scattered surface plasmon wave. Finite-difference time-domain simulation of the experimental PEEM imaging is in good agreement with the polarization gratings. It also explains the increase of the coupling efficiency as a result of the constructive interference between the incident wave and the scattered cylindrical wave inside the slit, which is dependent on the oblique incidence angle. Furthermore, the simulation results also show the slit width dependence of the backward scattered surface wave signal, the transmission through the slit, and the electromagnetic field distribution inside the slit, which are difficult to measure in the experiments. This work calls for further investigation of ultrafast surface plasmon wave dynamics, for example, the effects of other coupling geometries (such as slit arrays or grooves) and incidence conditions (such as pulse duration and incident angle), which point to interesting applications such as active control of surface plasmons.

Acknowledgments

This research was supported by NSF Grants CHE-0507147 and CHE-1012207, PRESTO JST, and the W. M. Keck Foundation. LXZ and TS thank İlker Çapoğlu for discussions.

[1] H. A. Atwater, *Sci. Am.* **296**, 56 (2007).

[2] J. M. Pitarke, V. M. Silkin, E. V. Chulkov, and P. M. Echenique, *Rep. Prog. Phys.* **70**, 1 (2007).

[3] T. W. Ebbesen, H. J. Lezec, H. F. Ghaemi, T. Thio, and P. A. Wolff, *Nature (London)* **391**, 667 (1998).

[4] L. Yin, V. K. Vlasko-Vlasov, A. Rydh, J. Pearson, U. Welp, S.-H. Chang, S. K. Gray, G. C. Schatz, D. B. Brown, and C. W. Kimball, *Appl. Phys. Lett.* **85**, 467 (2004).

[5] H. Ditlbacher, J. R. Krenn, G. Schider, A. Leitner, and F. R. Aussenegg, *Appl. Phys. Lett.* **81**, 1762 (2002).

[6] K. G. Lee and Q.-H. Park, *Phys. Rev. Lett.* **95**, 103902 (2005).

[7] J. Wuenschell and H. K. Kim, *Opt. Express* **14**, 10000 (2006).

[8] H. W. Kihm, K. G. Lee, D. S. Kim, J. H. Kang, and Q.-H. Park, *Appl. Phys. Lett.* **92**, 051115 (2008).

[9] B. Wang, L. Aigouy, E. Bourhis, J. Gierak, J. P. Hugonin, and P. Lalanne, *Appl. Phys. Lett.* **94**, 011114 (2009).

[10] H. W. Kihm, J. H. Kang, J. S. Kyoung, K. G. Lee, M. A. Seo, and K. J. Ahn, *Appl. Phys. Lett.* **94**, 141102 (2009).

[11] H.-W. Kihm, Q. H. Kihm, D. S. Kim, K. J. Ahn, and J. H. Kang, *Opt. Express* **18**, 15725 (2010).

[12] B. Ung and Y. Sheng, *Opt. Express* **15**, 1182 (2007).

[13] Y. S. Jung, J. Wuenschell, T. Schmidt, and H. K. Kim, *Appl. Phys. Lett.* **92**, 023104 (2008).

[14] H. Kim and B. Lee, *Plasmonics* **4**, 153 (2009).

[15] P.-K. Wei, Y.-C. Huang, C.-C. Chieng, F.-G. Tseng, and W. Fann, *Opt. Express* **13**, 10784 (2005).

[16] J. S. White, G. Veronis, Z. Yu, E. S. Barnard, A. Chandran, S. Fan, and M. L. Brongersma, *Opt. Lett.* **34**, 686 (2009).

[17] R. Gordon, *Phys. Rev. B* **73**, 153405 (2006).

[18] For a review, see F. J. Garcia-Vidal, L. Martin-Moreno, T. W. Ebbesen, and L. Kuipers *Rev. Mod. Phys.* **82**, 729 (2010).

[19] W. L. Barnes, A. Dereux, and T. W. Ebbesen, *Nature (London)* **424**, 824 (2003).

[20] M. Durach, A. Rusina, M. I. Stockman, and K. Nelson, *Nano Lett.* **7**, 3145 (2007).

[21] M. Sukharev and T. Seideman, *J. of Phys. B: At. Mol. Opt. Phys.* **40**, S283 (2007).

[22] R. F. Oulton, V. J. Sorger, D. A. Genov, D. F. P. Pile, and X. Zhang, *Nat. Photonics* **2**, 496 (2008).

[23] E. Ozbay, *Science* **311**, 189 (2006).

[24] H. A. Atwater and A. Polman, *Nat. Mater.* **9**, 205 (2010).

[25] G. Gay, O. Alloschery, B. Viaris de Lesegno, C. O'Dwyer, J. Wainer, and H. J. Lezec, *Nat. Phys.* **2**, 262 (2006).

[26] F. J. García-Vidal, S. G. Rodrigo, and L. Martín-Moreno, *Nat. Phys.* **2**, 790 (2006).

[27] J. Weiner and H. J. Lezec, *Nat. Phys.* **2**, 791 (2006).

[28] G. Gay, O. Alloschery, J. Weiner, H. J. Lezec, C. O'Dwyer, M. Sukharev, and T. Seideman, *Nat Phys.* **2**, 792 (2006).

[29] P. Lalanne, J.P. Hugonin, M. Besbes, and P. Bienstman, *Nat. Phys.* **2**, 792 (2006).

[30] C. Ropers, D. J. Park, G. Stibenz, G. Steinmeyer, J. Kim, D. S. Kim, and C. Lienau, *Phys. Rev. Lett.* **94**, 113901 (2005).

[31] see R. Müller and J. Bethge, *Phys. Rev. B* **82**, 115408 (2010) and references therein.

[32] A. M. Nugrowati, S. F. Pereira, and A. S. van de Nes, *Phys. Rev. A* **77**, 053810 (2008).

[33] D. K. Gramotnev and S. I. Bozhevolnyi, *Nat. Photonics* **4**, 83 (2010).

[34] K. F. MacDonald, Z. L. Sámson, M. I. Stockman, and N. I. Zheludev, *Nat. Photonics* **3**, 55 (2009).

[35] A. Kubo, K. Onda, H. Petek, Z. Sun, Y.-S. Jung, and H.-K. Kim, *Nano Lett.* **5**, 1123 (2005).

[36] A. Kubo, N. Pontius, and H. Petek, *Nano Lett.* **7**, 470 (2007).

[37] A. Kubo, Y. S. Jung, H. K. Kim, and H. J. Petek, *J. of Phys. B: At. Mol. Opt. Phys.* **40**, S259 (2007).

[38] V. V. Temnov, K. Nelson, G. Armelles, A. Cebollada, T. Thomay, A. Leitenstorfer, and R. Bratschitsch, *Opt. Express* **17**, 8423 (2009).

[39] J. Renger, R. Quidant, N. van Hulst, S. Palomba, and L. Novotny, *Phys. Rev. Lett.* **103**, 266802 (2009).

[40] M. Bauer, C. Wiemann, J. Lange, D. Bayer, M. Rohmer and M. Aeschlimann, *Appl. Phys. A* **88**, 473 (2007).

[41] L. I. Chelaru and F.-J. Meyer zu Heringdorf, *Surf. Sci.* **601**, 4541 (2007).

[42] A. Oelsner, M. Rohmer, C. Schneider, D. Bayer, G. Schonhense, and M. Aeschlimann, *J. Electron. Spectrosc. Relat. Phenom.* **178**, 317 (2010).

[43] B. Hecht, H. Bielefeldt, L. Novotny, Y. Inouye, and D. W. Pohl, *Phys. Rev. Lett.* **77**, 1889 (1996).

[44] L. Salomon, G. Bassou, H. Aourag, J. P. Dufour, F. de Fornel, F. Carcenac, and A. V. Zayats, *Phys. Rev. B* **65**, 125409 (2002).

[45] C. Timm and K. H. J. Bennemann, *J. of Phys.: Cond. Mat.* **16**, 661 (2004).

[46] I. Matsuda and H. W. Yeom, *J. Electron. Spectrosc. Relat. Phenom.* **126**, 101 (2002).

[47] H. Petek and A. Kubo, *Ultrafast microscopy of plasmon dynamics in nanostructured metal surfaces. In Handbook of Instrumentation and Techniques for Semiconductor Nanostructure Characterization*, edited by R. Haight, F. Ross, and J. Hannon (World Scientific Publishing/Imperial College Press) in press.

[48] N. Pontius, V. Sametoglu, and H. Petek, *Phys. Rev. B* **72**, 115105 (2005).

[49] P. B. Johnson and R. W. Christy, *Phys. Rev. B* **6**, 4370 (1972).

[50] At the two ends of the wavelength interval $330 \le \lambda_0 \le 500$ nm, to which the Drude model is fitted, the Fourier transform of this signal is 8.9×10^{-6} and 1.7×10^{-5}, respectively, of the peak value at $\lambda_0 = 400$ nm.

[51] L.-X. Zhang and T. Seideman, *Phys. Rev. B* **82**, 155117 (2010).

[52] A. Taflove and S. C. Hagness, *Computational Electromagnetics: The Finite-Difference Time-Domain Method,* 3rd ed. (Artech House, Boston, 2005).

[53] S. D. Gedney, Electromagnetics **16**, 399 (1996).

[54] The electric polarization vector is given by $\boldsymbol{P} = \boldsymbol{D} - \varepsilon_0 \boldsymbol{E}$, and both the electric displacement vector **D** and electric field **E** are obtained from the FDTD calculation.

[55] S.-H. Chang, S. K. Gray, and G. C. Schatz, *Opt. Express* **13**, 3150 (2005).

[56] O. T. A. Janssen, H. P. Urbach, and G. W.'t Hooft, *Opt. Express* **14**, 11823 (2006).

[57] J. Weiner, *Opt. Express* **16**, 950 (2008).

[58] P. Lalanne, J. P. Hugonin, and J. C. Rodier, *J. Opt. Soc. Am. A* **23**, 1608 (2006).

[59] L. Aigouy, P. Lalanne, J. P. Hugonin, G. Julié, V. Mathet, and M. Mortier, *Phys. Rev. Lett.* **98**, 153902 (2007).

[60] L.-X. Zhang, A. Kubo, H. Petek, and T. Seideman, unpublished.

FIGURES

FIG. 1. (a) The experimental light irradiation geometry and definition of the coordinate axes system. w, t, and θ indicate the slit width, the slit thickness (80 nm), and the light angle of incidence (65°), respectively. (b) PEEM image of a 200 nm slit taken with Hg-lamp incident from the right side showing the morphology and position of slit. (c) PEEM image taken with 10 fs, 400 nm light pulse excitation incident from the left side. (d) The cross section of the PEEM image in (c) after averaging along the z-direction. (e) Simulated polarization grating pattern. The dotted line shows the beat pattern calculated for cw-light excitation. Calculations in (e) are based on the analytical model of Sec. III A.

FIG. 2. (Color online) Schematic illustration of the FDTD simulation set up. A p-polarized plane wave is incident at θ=65° from the normal of an Ag thin film of thickness t=80 nm. A vacuum slit of width w is placed in the middle of the film. Forward scattering, backward scattering, and transmission through the slit are denoted by *FSC*, *BSC,* and *T*, respectively. The total field (scattered field) region is inside (outside) the shaded area enclosed by the thick dashed rectangle. The two outermost rectangles show the inner and outer boundaries of the UPML. The blue, horizontal dashed-dotted and dotted lines denote detection lines at the top surface and across the slit at the bottom. The dimensions are not to scale.

FIG. 3. (Color online) (a) Slit width dependence of the polarization grating pattern. (b) The red solid line shows the intensity of the first peak of each beat trace. The dotted line underneath it shows a generally increasing trend. The blue dotted line shows the same data with the intensities converted to magnitudes of the SPP excitation parameter, β. Arrows point to slit widths $w_n = n\lambda_0/2$, which correspond to positions of the local intensity maxima.

FIG. 4. (a) Selected profiles of the polarization beat patterns; and (b) the corresponding simulations using the analytical model.

FIG. 5. (Color online) (a) Main panel: calculated interference patterns at the top surface. The red (boldest) curve shows the time-integrated signal $I_s(x)$ in the case of Gaussian-pulse illumination. The blue (black, thinnest) curve shows the time-average signal $\overline{P_{total}^4(x)}$ in the case of continuous wave illumination for Ag film of thickness 80 (200) nm. The three interference patterns are aligned to the slit right edge ($x=0$) and normalized to unity at the first peak to the right of the slit. Upper left inset: expanded view near the left edge of the slit. Upper right inset: expanded view of the red curve for $3<x<10$ μm. Arrows and numbers in circles indicate features that are discussed in the text. (b) Top surface interference signal $I_S(x,t)$ and surface magnetic fields $H_S(x,t)$ of the incident (dashed curve) and the pure scattered (solid curve) surface waves as functions of x distance at t=9.321 fs after the peak of an oblique Gaussian pulse passes the right edge of a slit with w=200 nm.

FIG. 6. (Color online) (a) Interference signals at the first peak to the left (green curve, with superimposed squares) and right (red curve, with superimposed dots) of the slit as functions of the slit width w. (b) Total transmission normalized to the slit width T_{total}/w (blue, with superimposed asterisks) as a function of the slit width w.

FIG. 7. (Color online) Distribution of E_y and H_z field components (time-integrated values of E_y^2 and H_z^2) in the vicinity of the slit for (a) slit width w=λ_0/2=200 nm, corresponding to the first Fabry-Pérot cavity mode. (b) w=5λ_0/4=500 nm, corresponding to a cavity anti-resonance, and (c) w=3λ_0/2=600 nm, corresponding to the third Fabry-Pérot cavity mode. A log (linear) color scale is used for E_y^2 (H_z^2). The Ag slabs are indicated by thick dashed gray rectangles. The dashed circles highlight the modulation of H_z^2 field at the left edge of the slit.

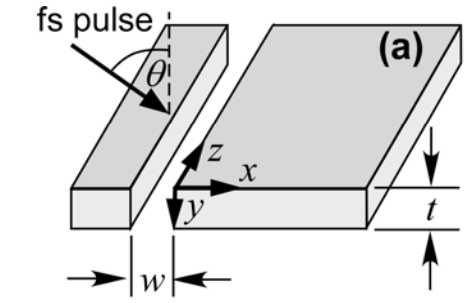
fs pulse
θ
(a)
z
x
y
t
w

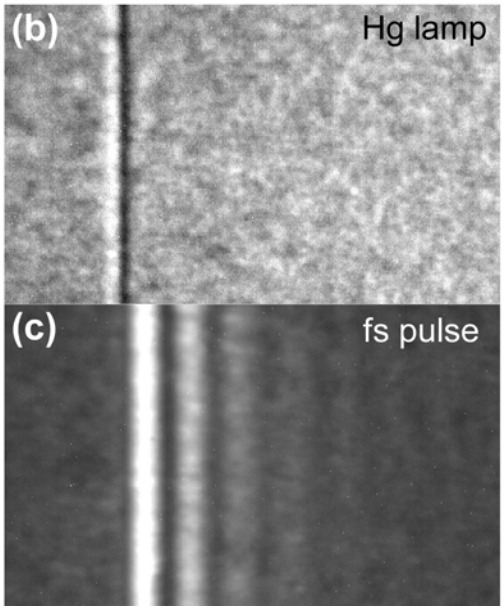
(b)
Hg lamp
(c)
fs pulse

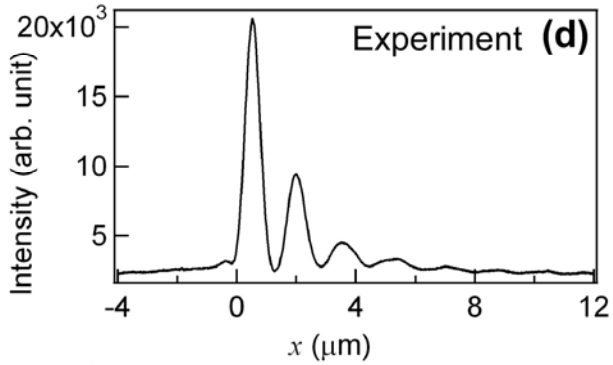
20x10^3
15
10
5
Intensity (arb. unit)
Experiment
(d)
-4
0
4
8
12
x (μm)

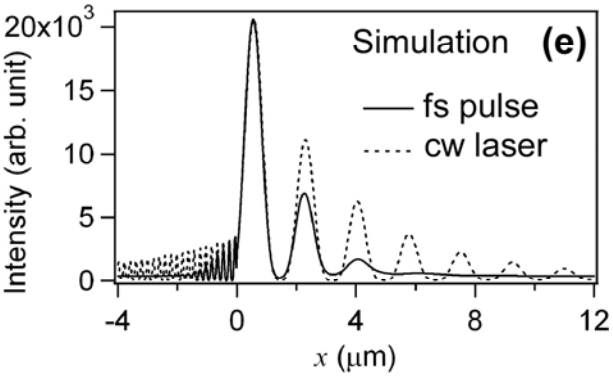
20x10^3
15
10
5
0
Intensity (arb. unit)
Simulation
(e)
fs pulse
cw laser
-4
0
4
8
12
x (μm)

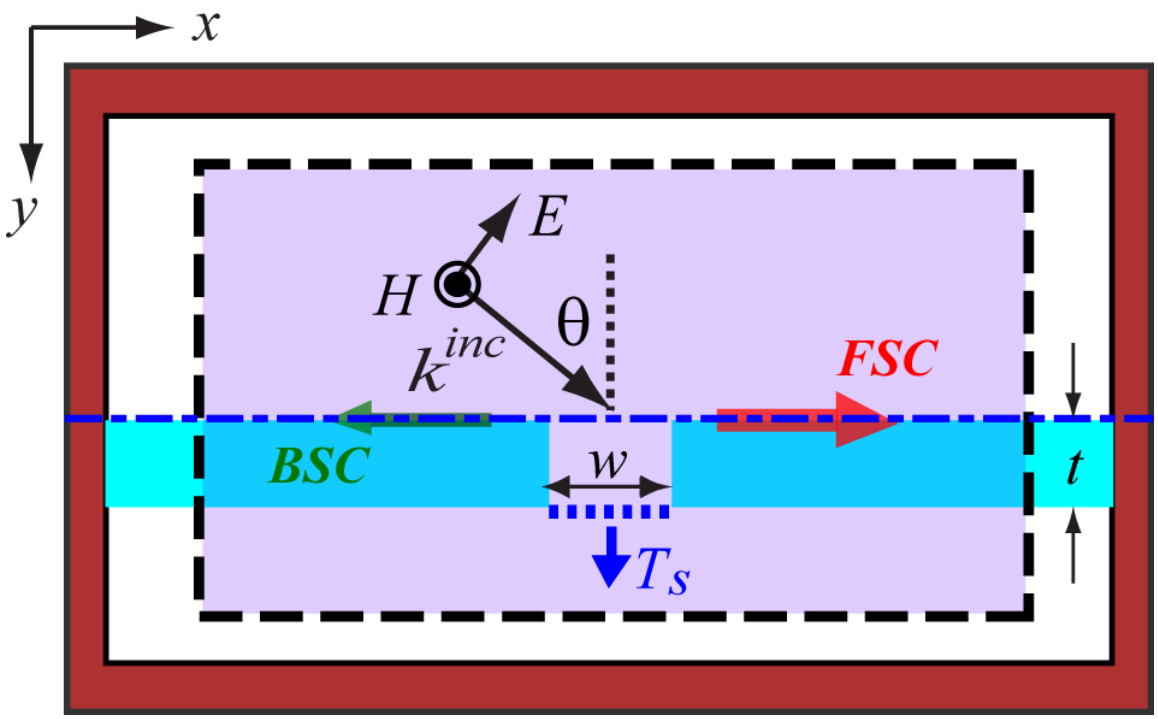
x
y
E
H
θ
k^inc
FSC
BSC
w
t
T_s

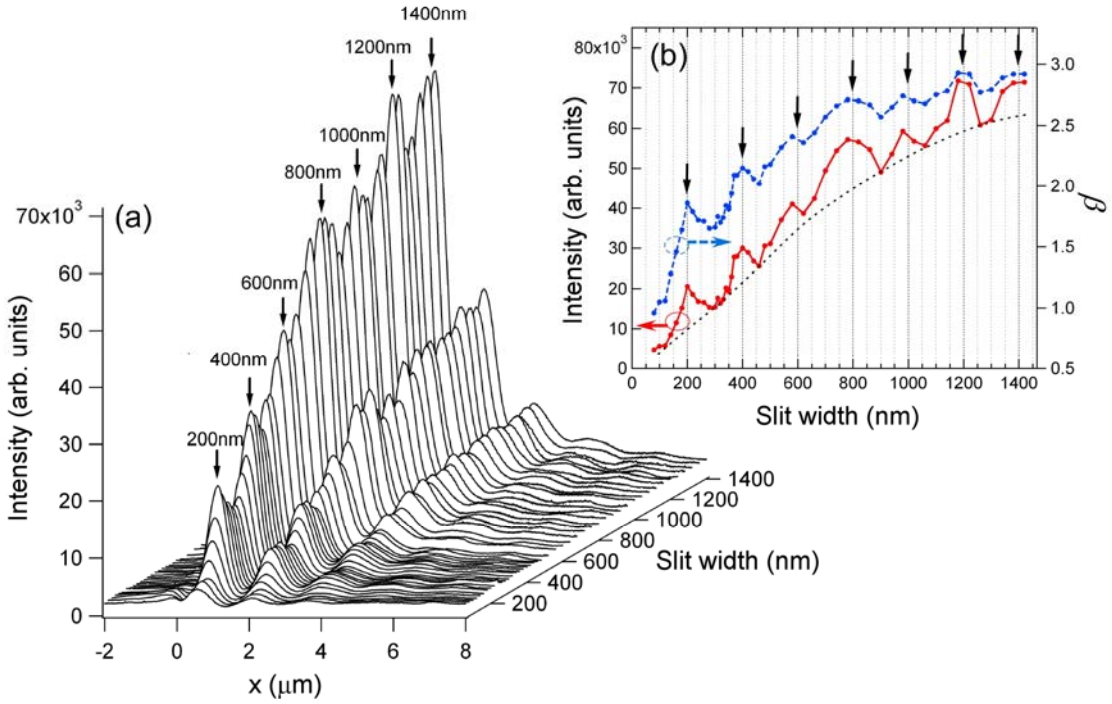
(a)
70x10^3
Intensity (arb. units)
60
50
40
30
20
10
0
-2
0
2
4
6
8
x (μm)
1400nm
1200nm
1000nm
800nm
600nm
400nm
200nm
1400
1200
1000
800
600
400
200
Slit width (nm)
(b)
80x10^3
Intensity (arb. units)
70
60
50
40
30
20
10
0
200
400
600
800
1000
1200
1400
Slit width (nm)
3.0
2.5
2.0
1.5
1.0
0.5
β

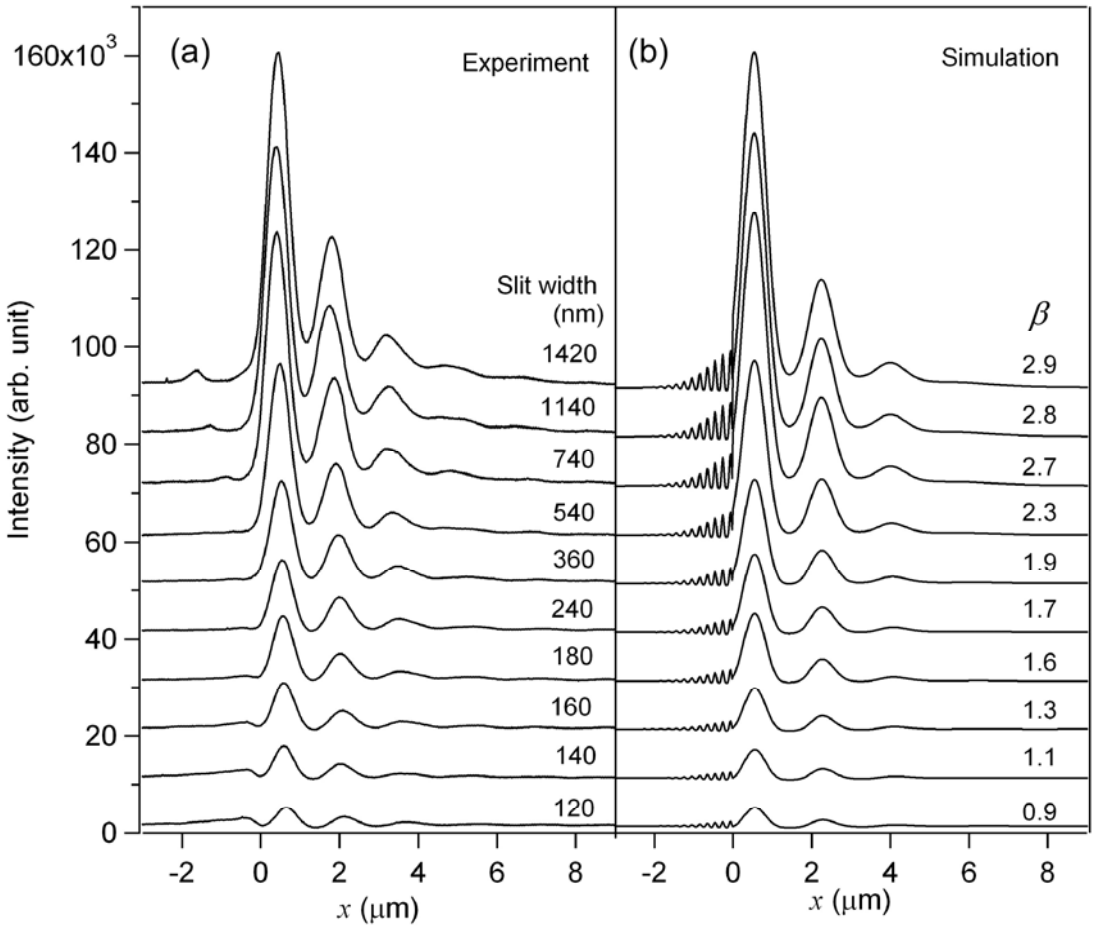
(a)
Experiment
(b)
Simulation
160x10^3
140
120
100
80
60
40
20
0
Intensity (arb. unit)
Slit width (nm)
1420
1140
740
540
360
240
180
160
140
120
β
2.9
2.8
2.7
2.3
1.9
1.7
1.6
1.3
1.1
0.9
-2
0
2
4
6
8
x (μm)

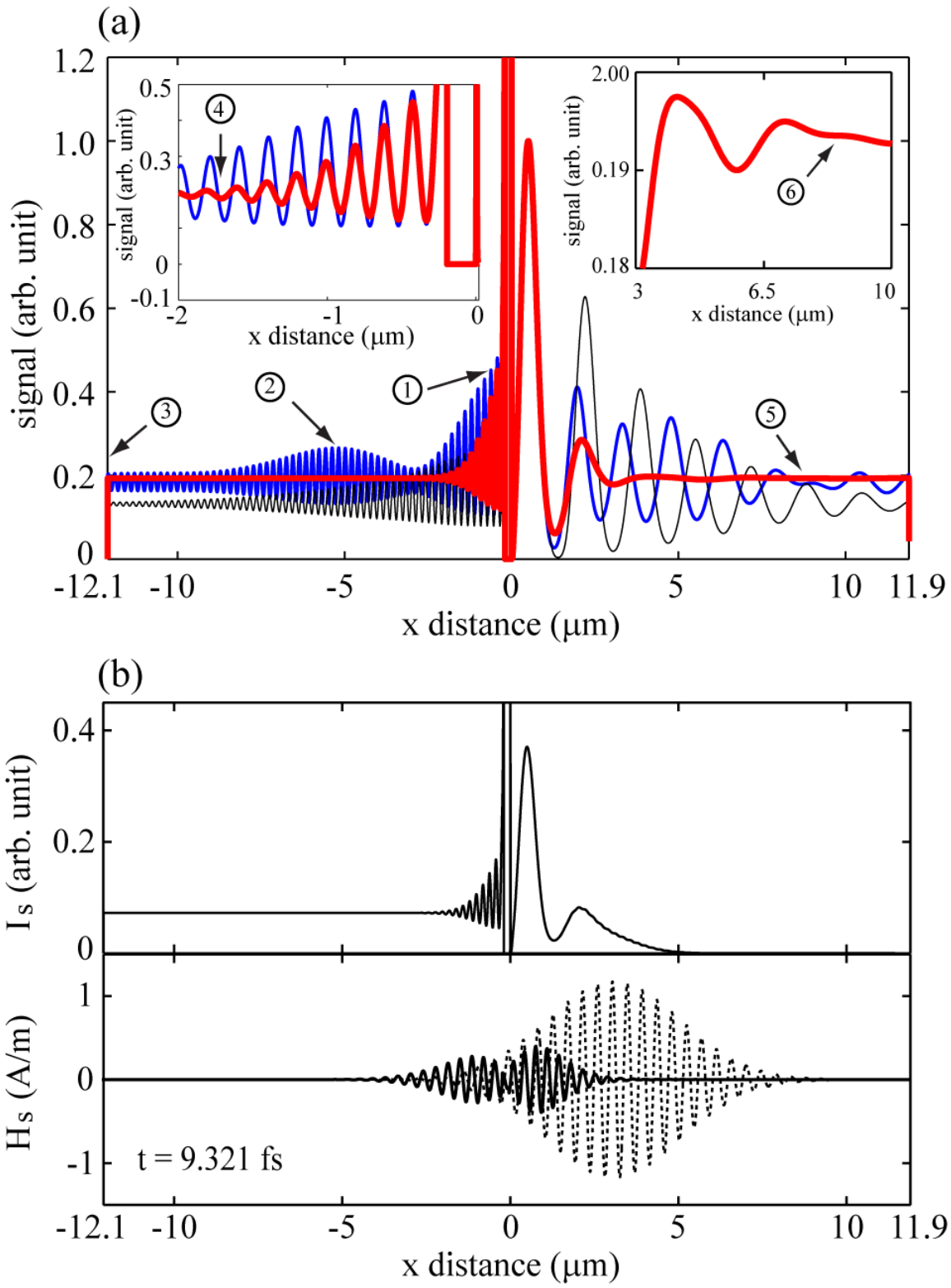
(a)
signal (arb. unit)
x distance (μm)
1.2
1.0
0.8
0.6
0.4
0.2
0
-12.1
-10
-5
0
5
10
11.9
①
②
③
④
⑤
⑥
0.5
0.3
0
-0.1
-2
-1
0
2.00
0.19
0.18
3
6.5
10
(b)
Is (arb. unit)
Hs (A/m)
0.4
0.2
1
-1
t = 9.321 fs

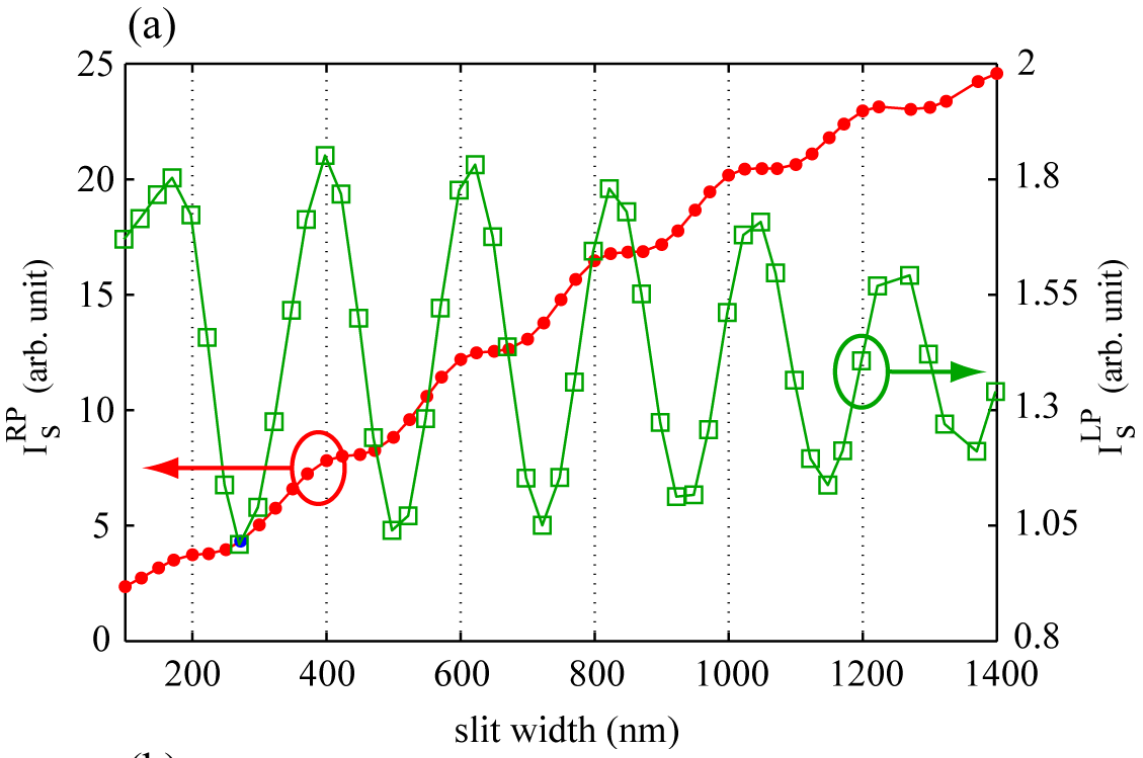
(a)
25
20
15
10
5
0
2
1.8
1.55
1.3
1.05
0.8
200
400
600
800
1000
1200
1400
slit width (nm)
I_S^{RP} (arb. unit)
I_S^{LP} (arb. unit)

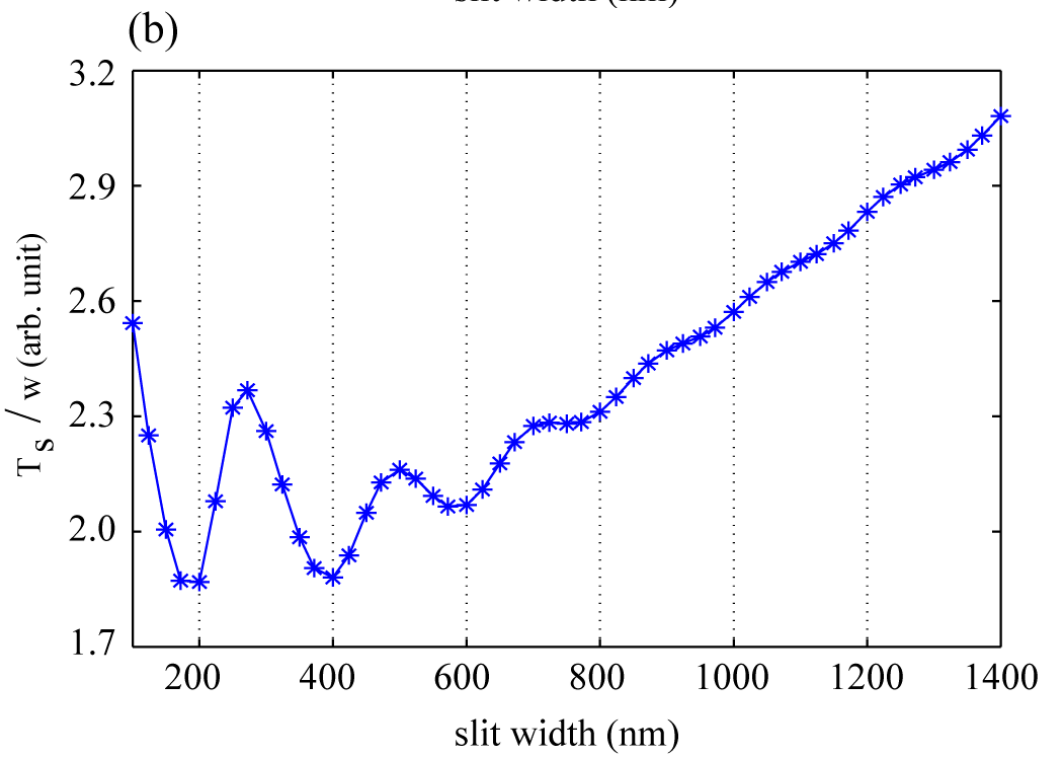
(b)
3.2
2.9
2.6
2.3
2.0
1.7
200
400
600
800
1000
1200
1400
slit width (nm)
T_S / w (arb. unit)

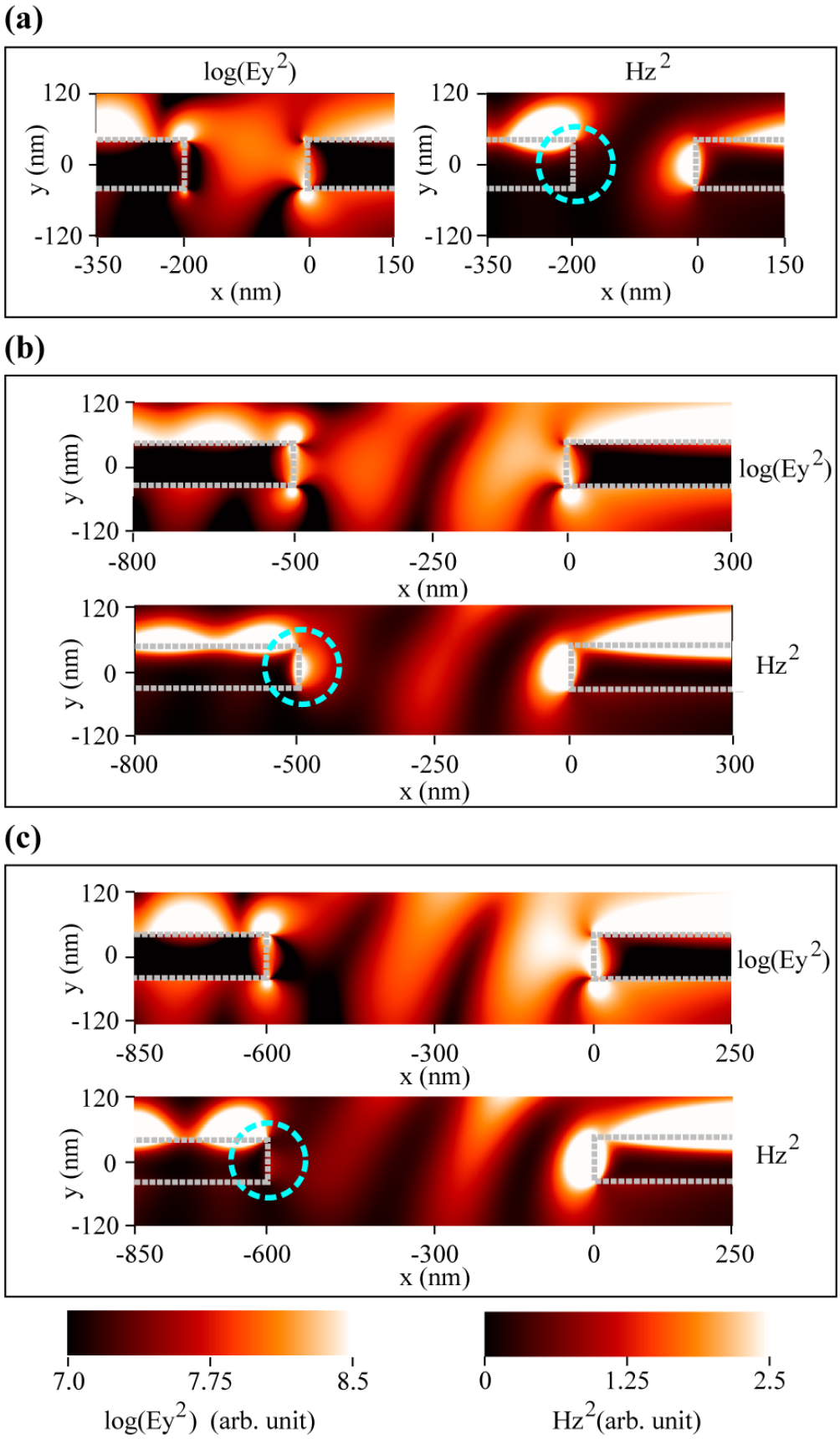
(a)
log(Ey2)
Hz2
120
0
-120
y (nm)
-350
-200
0
150
x (nm)
(b)
-800
-500
-250
300
(c)
-850
-600
-300
250
7.0
7.75
8.5
log(Ey2) (arb. unit)
0
1.25
2.5
Hz2(arb. unit)